Progress In Electromagnetics Research M, Vol. 13, 1–16, 2010

RIGOROUS 3D VECTORIAL GAUSSIAN BEAM MODELING OF DEMULTIPLEXING PERFORMANCE OF VIRTUALLY-IMAGED-PHASED-ARRAYS

A. Mokhtari and A. A. Shishegar

Dept. of Electrical Engineering
Sharif University of Technology
Azadi Avenue, Tehran, Iran

Abstract—We extend our previously-derived generalized closed-form representation for spectral dispersing performance of the Virtually-Imaged-Phased-Array (VIPA) based on a 3D vectorial Gaussian beam formulation to demultiplexing application. To analyze VIPA in the demultiplexer scheme, a spherical lens is added after the VIPA, so that the device plane is superimposed on the focal plane of the lens. The calculated output profile at previous step is reformulated ¿ in a matrix form in this step. Finally, the derived closed-form is simulated, and the numerical outcomes are compared with the previous results. The 3D output radiation of VIPA demultiplexer pattern is also depicted and found to be very intuitive and promising for some applications especially WDM demultiplexer and optical Code Division Multiple Access (CDMA).

1. INTRODUCTION

Multiplexing/demultiplexing devices are employed to separate and recombine optical wavelengths. There are two methods used to split the optical channels, one by cascaded splitting such as fiber Bragg grating or multilayer interference thin film [1] and the other by single multi-channel devices such as arrayed waveguide grating (AWG) [2, 3]. The former method is less favorable due to additive loss and noise. Finer spectral resolution is of the utmost importance in the development of hyperfine wavelength demultiplexing.

Recently, a modified and tilted version of etalon has been proposed and is found to be the best choice to replace the former MUX/DEMUX technologies especially to achieve narrower

Corresponding author: A. Mokhtari (amokhtari@ee.sharif.edu).

channel widths in hyperfine WDM schemes. This device shows high angular dispersion (for example 0.5 deg/nm) which is high enough to be utilized in 0.8 nm channel spacing WDM [4–7]. This device is utilized in many applications, such as chromatic dispersion compensation [5, 6], direct space-to-time pulse shaping [8], OCDMA encoder/decoder [9], photonic-microwave arbitrary waveform generation [10] and programmable optical burst manipulation [11].

The VIPA principal demultiplexing system is depicted in Figure 1. The VIPA operation can be explained based on the Fabry-Perót etalon. It consists of two high reflective coated planes. The input (entry) side has a reflectivity factor close to 1.0 except at a window that remains uncoated or coated with anti-reflection (AR) material to allow light beam entrance. The laser source beam is focused on the output plate of the etalon by a proper lens (mostly a semi-cylindrical one). The collimated beam enters the etalon through the window and reflects back and forth. The round-trip beam is partly reflected and transmitted, and the reflection continues until all injected power leaks out of the etalon. The resulted diverging beams from virtual sources (VSs) interfere with each other in a phased array and form a collimated beam. The phase differences between the diverging beams are highly dependant on the wavelength variations; hence, the VIPA disperses the beam angularly. Then, the spherical lens is used to focus the generated diverging beams on the fiber array to discriminate the wavelengths. In other words, the lens imaging system collimates the beams of different wavelengths on the different points of the lens focal plane. Consequently, each wavelength enters a unique fiber in fiber detector array. The VIPA surpasses the common diffraction gratings due to several advantages such as large angular dispersion, low polarization sensitivity, simple structure, compactness and better performance [7].

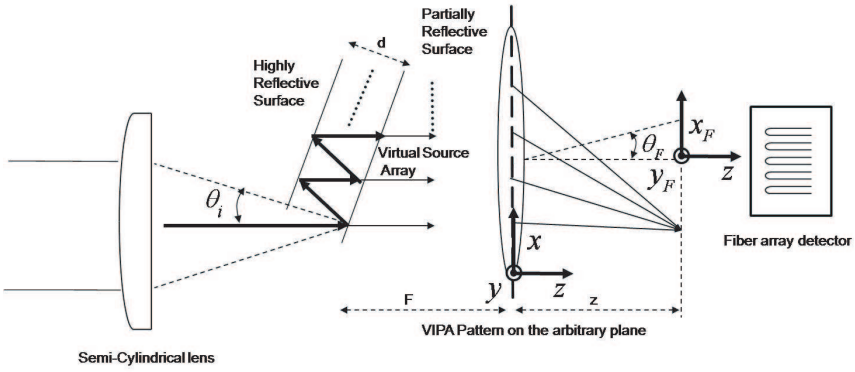

Figure 1. The setup used to analyze the VIPA demultiplexer.

Function of VIPA after the lens (in a demultiplexer scheme) was first characterized numerically in [4, 7] by Shirasaki. Pioneer analytical approach by Yang [12] modeled VIPA as a periodic filter and described the maxima of pass bands as a function of diffraction angle using 2D Gaussian beam and Fourier transform. Vega [13] proposed a grating equation based on a plane wave theory for relatively large incident angles. Xiao [14] considered the paraxial waves and generalized the Vega's approach for small incident angles. Later, he provided an analytical expression for the pass band response of VIPA demultiplexers [15].

All the above mentioned analytical approaches treat the VIPA with a 2D, scalar model, while neglecting the vertical profile variations, collimation effect of spherical lens in transverse plane and TE/TM different reflection/transmission coefficients. All supposed that the input beam is focused exactly on the outer side, and keep the output reflection profile constant over the whole surface (except [4, 7]) despite the fact that this profile can be engineered to optimize the VIPA performance. Here, trying to eliminate the previous restricting assumptions, we follow our rigorous 3D vectorial Gaussian beam method from [16, 17] to extend our previous spectral dispersing framework and find a detailed matrix representation of VIPA demultiplexer output pattern. A generalized imaging lens is employed where input field is placed against the lens and pattern variations due to changing imaging parameters are investigated.

This paper is structured as follows: Section 2 includes the derivation of vectorial Gaussian beam description of pattern formulation after the lens; Section 3 contains numerical results of the extracted equations for the comparison of VIPA demultiplexer performance with the previous works and the related discussions. Finally, we conclude in Section 4.

2. THEORETICAL DERIVATION

We had previously derived the closed form representation of VIPA pattern on arbitrary parallel plane after the device [16, 17]. We deal with the new problem in the following approach: The arbitrary plane is selected deliberately to superimpose on the lens one and the field pattern is calculated; then, we apply the imaging function of the lens on the pattern employing the Fresnel complex 2D integration. Finally, by acquiring each virtual source pattern after the lens, the final pattern is represented in closed-form on an arbitrary distance after the lens.

Suppose Figure 1 is used for the analysis of device performance. We have some assumptions in calculation procedure: First, due to

nonlinear phase of Gaussian beam propagation from the lens plane, the propagation phase can not be measured by $\exp(-jk_2d)$ similar to a plane wave (d is the distance between the lens and observation point). The propagation variations are fully considered in the Gaussian beam term. Second, the lens diameter is much larger than the object. So the lens pupil function is close to 1 [18]. Third, we consider the lens spatial and temporal phasor term with the convention $\exp(j\omega t - jkz)$ that will be employed in final field representation. Forth, we use the paraxial approximation to derive the field after the lens. Finally, we assume that both the lens focal plane and the detector point satisfy the Fresnel condition [18]. In order to derive the field pattern after the lens at an arbitrary distance, we calculate the Fresnel integration for $z \geq z_{\min}$ where $z_{\min}$ is dictated by the lower bound of Fresnel condition.

2.1. Final Field Calculations

If field pattern before the spherical lens (with focal length F) showed by $U_l(x,y)$, the lens functions as a phase mask of $\exp(j\frac{k_2}{2F}(x^2+y^2))$; hence, the field after the lens is obtained through multiplying the field before the lens by the lens phase function:

$$U(x,y) = U_l(x,y) \times \exp\left(j\frac{k_2}{2F}\left(x^2+y^2\right)\right) \tag{1}$$

Field pattern is a function of both transverse coordinate system (x,y) and the propagation direction z; thus, the field can be expanded by dividing it into the propagation and the transverse terms as follows:

$$U_l(x,y,z) = \sum_{m=1}^{N} E_{tot,m}(z) \times \exp\left\{-j\frac{k_2}{2}q_m^f(x,y)\right\} \tag{2}$$

where $E_{tot,m}(z)$ and $q_m^f(x,y)$ are the field of the mth virtual source and q-parameter of Gaussian beam respectively [17]. We define some parameters for mth virtual source before proceeding:

$$\begin{aligned}\mathbf{Q_m^i} = & Rot(\alpha_3) \\ & \times \begin{pmatrix} \left\{F_x(q_{x_{3m-1}}(0), q_{y_{3m-1}}(0)) + Z_{Pm}\right\}^{-1} & 0 \\ 0 & \left\{F_y(q_{x_{3m-1}}(0), q_{y_{3m-1}}(0)) + Z_{Pm}\right\}^{-1} \end{pmatrix} \\ & \times Rot(-\alpha_3)\end{aligned} \tag{3a}$$

While, we have:

$$Z_{Pm} = (N-m+1) \times 2d\tan(\theta_i)\cos(\varphi) \tag{3b}$$

$$F_{\underset{y}{x}}\{q_{x_{3m-1}}(0), q_{y_{3m-1}}(0)\} = \frac{2\frac{k_2}{k_1}q_{x_{3m-1}}(0)q_{y_{3m-1}}(0)}{\xi \pm \sqrt{\xi^2 - 4\beta^2 q_{x_{3m-1}}(0)q_{y_{3m-1}}(0)}} \tag{3c}$$

where:

$$\begin{cases} \xi = \left(\beta^2 \sin^2(\alpha_1) + \cos^2(\alpha_1)\right) q_{x_{3m-1}}(0) \\ \quad + \left(\beta^2 \cos^2(\alpha_1) + \sin^2(\alpha_1)\right) q_{y_{3m-1}}(0) \\ \beta = \cos(\theta_i)/\cos(\theta_t) \\ q_{x_{3m-1}}(0) = q_{x_1}(Z_0) + 2(m-1)d/\cos(\theta_i) \\ q_{y_{3m-1}}(0) = q_{y_1}(Z_0) + 2(m-1)d/\cos(\theta_i) \end{cases} \tag{3d}$$

The θ_i and θ_t are incident and transmitted angles. $Rot(\alpha_3)$ is the rotation matrix by angle α_3 as depicted in Figure 2. k_i is the propagation constant for the ith medium equal to $\omega\sqrt{\varepsilon_i \mu_i}$. N, d and $q_{i_j}(z)$ are total number of virtual sources, VIPA thickness, and the jth Gaussian beam q parameter at z for $i = x$ or y directions respectively.

By considering D (the lens diameter) and correct transformation of field from coordinate system (x, y, z) to lens plane coordinate system by a $D/2$ shift, $q_m^f(x, y)$ is calculated from the following equation:

$$\begin{aligned} -\frac{jk_2}{2} q_m^f(x, y) &= [x - x_m \; y] \mathbf{Q_m^i} [x - x_m \; y]^t \\ &= a(x - x_m)^2 - jb(x - x_m)y + cy^2 \end{aligned} \tag{4a}$$

$$\begin{cases} x_m = (m-1)2d \tan(\theta_i) \sin(\varphi) - \dfrac{D}{2} \\ a = -j\dfrac{k_2}{2} \mathbf{Q_m^i}(1,1) \\ b = \dfrac{k_2}{2} \left\{ \mathbf{Q_m^i}(1,2) + \mathbf{Q_m^i}(2,1) \right\} = k_2 \mathbf{Q_m^i}(1,2) \\ c = -j\dfrac{k_2}{2} \mathbf{Q_m^i}(2,2) \end{cases} \tag{4b}$$

$\mathbf{Q_m^i}(i, j)$ is the element in ith row and jth column of $\mathbf{Q_m^i}$ matrix. Because the final term in Eq. (2) is only the function of transverse coordinate system (z), the integration operator enters the summation and operates on the $q_m^f(x, y)$ term that is described as follows in the lens coordinate system (x_F, y_F):

$$U_l(x_F, y_F, z) = \sum_{m=1}^{N} E_{tot,m}(z) \times U_f(x_F, y_F, z) \tag{5}$$

While $U_f(x_F, y_F, z)$ is field pattern of each virtual source after the lens. This relation remains true for arbitrary vertical plane parallel to the focal plane until the Fresnel lower boundary satisfied ($z \geq$

$z_{\min}$). The field after the lens is derived through Fourier transforms integration [18–21]:

$$U_f(x_F,y_F,z)=\exp\!\left(-j\frac{k_2}{2z}\left(x_F^2+y_F^2\right)\right)\times\frac{\exp(-jk_2z)}{j\lambda z}\times\int_{-\infty}^{\infty}\int_{-\infty}^{\infty}\exp\!\left\{-j\frac{k_2}{2}q_m^f(x,y)\right\}\times\exp\!\left\{j\frac{k_2}{2F}\left(x^2+y^2\right)\right\}\times\exp\!\left\{-j\frac{k_2}{2z}\left[(x_F-x)^2+(y_F-y)^2\right]\right\}dxdy \tag{6}$$

That simplified as follows:

$$U_f(x_F,y_F,z)=\exp\!\left(-j\frac{k_2}{z}\left(x_F^2+y_F^2\right)\right)\times\frac{\exp(-jk_2z)}{j\lambda z}\times\int_{-\infty}^{\infty}\int_{-\infty}^{\infty}\exp\!\left\{-j\frac{k_2}{2}q_m^f(x,y)\right\}\times\exp\!\left\{j\frac{k_2}{z}(xx_F+yy_F)\right\}\times\exp\left\{j\frac{k_2}{2}\left(x^2+y^2\right)\left(\frac{1}{F}-\frac{1}{z}\right)\right\}dxdy \tag{7}$$

If we called $\Delta=\frac{1}{F}-\frac{1}{z}$ then in Fourier plane with coordinate system (x_F,y_F) the term is expanded using Eq. (4a) as:

$$U_f(x_F,y_F,z)=\frac{\exp\left(-jk_2z\right)}{j\lambda z}\times\exp\!\left(-j\frac{k_2}{z}\left(x_F^2+y_F^2\right)\right)\times\int_{-\infty}^{\infty}\int_{-\infty}^{\infty}\exp\!\left\{a(x-x_m)^2-jb(x-x_m)y+cy^2+j\frac{k_2}{z}(xx_F+yy_F)+j\frac{k_2}{2}\Delta\left(x^2+y^2\right)\right\}dxdy \tag{8}$$

The following complex integration formula is widely used:

$$\int_{-\infty}^{\infty}\exp\left(-\beta(x+\alpha)^2\right)\times\exp(-j\omega x)dx=\begin{cases}\sqrt{\dfrac{\pi}{\beta}}\times\exp\left(j\omega\left(\alpha+\dfrac{j\omega}{4\beta}\right)\right) & \text{complex sign }(\beta)=1\\ \text{Undefined} & \text{otherwise}\end{cases} \tag{9}$$

Complex sign (signum) is a symbolic function frequently employed in the mathematical toolboxes such as MATLAB or Maple. The square root of β remains unique with this criterion:

$$\text{complex sign}(\beta)=1\Rightarrow\begin{cases}\text{Re}(\beta)>0\\ \text{If Re}(\beta)=0\Rightarrow\text{Im}(\beta)>0\end{cases} \tag{10}$$

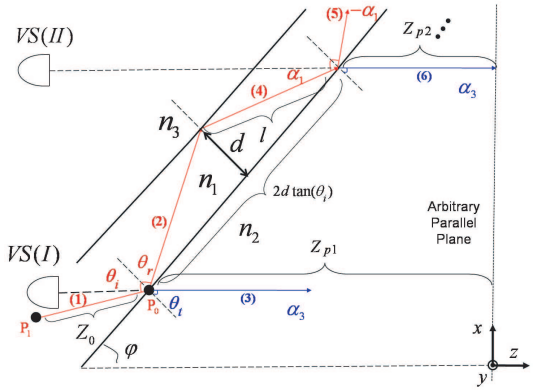

Figure 2. VIPA structure and the equivalent virtual sources.

After a lengthy calculation using complex Fourier integration and employing two stability criteria, the field after the lens on the focal plane is shown to be:

$$U_f(x_F, y_F, z) = \frac{\exp(-jk_2 z)}{j\lambda z} \times \exp\left(-j\frac{k_2}{z}\left(x_F^2 + y_F^2\right)\right) \times \exp\left(ax_m^2\right) \times \frac{\pi}{\sqrt{MK}} \exp\left(-\frac{1}{4}\left(\frac{L^2}{K} + \frac{N^2}{M}\right)\right) \quad (11)$$

where the K, L, M and N are the x^2, x, y^2 and y coefficients in Eq. (8) respectively:

$$\begin{cases} K = a + j\dfrac{k_2}{2}\Delta \\ L = -2ax_m + j\dfrac{k_2}{z}x_F \\ M = c + j\dfrac{k_2}{2}\Delta + \dfrac{b^2}{4K} \\ N = jbx_m + j\dfrac{k_2}{z}y_F + j\dfrac{bL}{2K} \end{cases} \quad (12)$$

With two stability criteria are defined as:

$$\begin{cases} \text{complex sign } (-M) = 1 \\ \text{complex sign } (-K) = 1 \end{cases} \quad (13)$$

If we summarize the matrix $\mathbf{Q_m^i} = Rot(\alpha_3)\begin{pmatrix} q_{x3m}^{-1} & 0 \\ 0 & q_{y3m}^{-1} \end{pmatrix} Rot(-\alpha_3)$, and by definition of a new parameter, $O = (\Delta - q_{x3m}^{-1})(\Delta - q_{y3m}^{-1})$, we

obtain the following equation:

$$\det\left(\mathbf{Q_m^i}\right) = (q_{x_{3m}} q_{y_{3m}})^{-1} \tag{14}$$

The analytical pattern of each virtual source after the demultiplexer on an arbitrary plane is derived:

$$\begin{aligned} U_f(x_F, y_F, z) = & \frac{\exp(-jk_2 z)}{z} \times \frac{\exp\left(-j\frac{k_2}{z}\left(x_F^2+y_F^2\right)\right)}{\sqrt{O}} \\ & \times \exp\Bigg(\frac{jk_2}{2O}\Bigg\{\begin{bmatrix}\frac{x_F}{z}\\ \frac{y_F}{z}\end{bmatrix}^t \begin{pmatrix} O+\mathbf{Q_m^{i2}}(1,2) & -\mathbf{Q_m^i}(1,2) \\ -\mathbf{Q_m^i}(2,1) & \mathbf{Q_m^i}(1,1)-\Delta \end{pmatrix} \begin{bmatrix}\frac{x_F}{z}\\ \frac{y_F}{z}\end{bmatrix} \\ & +2x_m \begin{bmatrix}\frac{x_F}{z}\\ \frac{y_F}{z}\end{bmatrix}^t \begin{pmatrix} \frac{O\mathbf{Q_m^i}(1,1)+\Delta\mathbf{Q_m^{i2}}(1,2)}{\mathbf{Q_m^i}(1,1)-\Delta} \\ -\Delta\mathbf{Q_m^i}(1,2) \end{pmatrix} \\ & +x_m^2\left(\frac{\Delta O\mathbf{Q_m^i}(1,1)+\Delta\mathbf{Q_m^{i2}}(1,2)}{\mathbf{Q_m^i}(1,1)-\Delta}\right)\Bigg\}\Bigg) \end{aligned} \tag{15}$$

For special case where the detector is on the focal plane ($z = F$), two defined parameters are simplified as follows:

$$\begin{cases} \Delta = \dfrac{1}{z} - \dfrac{1}{F} = 0 \\ O = (q_{x_{3m}}\ q_{y_{3m}})^{-1} = \det\left(\mathbf{Q_m^i}\right) \end{cases} \tag{16}$$

Consequently, each virtual source field on focal plane does not have the quadratic phase function:

$$\begin{aligned} U_f(x_F, y_F, z) = & \frac{\exp(-jk_2 F)}{F} \times \frac{\exp\left(-j\frac{k_2}{F}\left(x_F^2+y_F^2\right)\right)}{\sqrt{\det(\mathbf{Q_m^i})}} \\ & \times \exp\left(\frac{jk_2}{2}\left\{\begin{bmatrix}\frac{x_F}{F}\\ \frac{y_F}{F}\end{bmatrix}^t \mathbf{Q_m^i} - 1 \begin{bmatrix}\frac{x_F}{F}\\ \frac{y_F}{F}\end{bmatrix} + 2x_m\frac{x_F}{F}\right\}\right) \end{aligned} \tag{17}$$

The total field is found by summing up over each virtual source that can be showed as:

$$U_l(x_F, y_F, z) = \sum_{m=1}^{N} E_{tot,m}(z) \times U_f(x_F, y_F, z) \tag{18}$$

2.2. Discussion on Stability Criteria

In order to find the validity limits of two calculations, we use the following criteria (from Fresnel approximation) [18]:

$$z^3 \gg \frac{\pi}{4\lambda}\left\{(x-x_F)^2+(y-y_F)^2\right\}^2_{\max} \tag{19}$$

So, we should find the maximum for the second term:

$$\begin{aligned} &\max\left\{(x-x_F)^2+(y-y_F)^2\right\} \\ &= \max\left\{(x-x_F)^2\right\}+\max\{(y-y_F)^2\} = 2\left(\frac{D}{2}\right)^2 = \frac{D^2}{2} \end{aligned} \quad (20)$$

where D is the lens diameter. We extract the following lower limit for distance:

$$z \gg z_{\min} = \sqrt[3]{\frac{\pi}{4\lambda}\left(\frac{D^2}{2}\right)^2} = \sqrt[3]{\frac{\pi D^4}{16\lambda}} \quad (21)$$

For example if the lens diameter $D = 1\,\text{cm}$ and $\lambda = 1.55\,\mu\text{m}$, the lower limit is:

$$z \gg z_{\min} = \sqrt[3]{\frac{\pi \times 10^{-8}}{16 \times 1.55 \times 10^{-6}}} = 10.8\,\text{cm} \quad (22)$$

This limit is not exact and the derived formula is a good approximation for much less distances including stability criterion [18].

$$\text{complex sign}\ (-M) = 1 \Rightarrow \begin{cases} \text{Re}(-M) > 0 \\ \text{Re}(-M) = 0 \Rightarrow \text{Im}(-M) > 0 \end{cases} \quad (23)$$

And the other stability criterion is:

$$\text{complex sign}\ (-K) = 1 \Rightarrow \begin{cases} \text{Re}(-K) > 0 \\ \text{Re}(-K) = 0 \Rightarrow \text{Im}(-K) > 0 \end{cases} \quad (24)$$

These stability criteria are comparable to those derived in [22]. The condition is derived by limiting the response to the group of Gaussian beams that have decreasing amplitudes. These criteria should be checked to ensure that the solution remains in feasible region of Gaussian beams.

2.3. VIPA Demultiplexer Performance Figures of Merit

Two major dominating figures of merit (FOM) of every periodic (comb) filter are Free Spectral Range (FSR) and FWHM (3-dB bandwidth) that are depicted in Figure 3.

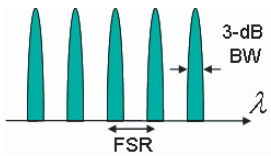

Figure 3. Periodic filter and main describing figures of merit.

2.3.1. FSR (Free Spectral Range)

The maximum width of spectrum span that can be determined without ambiguity is called the free spectral range [23]. Also, by definition, FSR is the frequency span of the input signal that the spectrum is reconstructable [24]. For the general case the FSR can be measured from transmission spectrum plot. The final field formula is derived as follows:

$$U_l(x_F,y_F,F)=\sum_{m=1}^{N}E_{tot,m}(F)\times\frac{\exp(-jk_2F)}{F}\times\frac{\exp\left(-j\frac{k_2}{2F}\left(x_F^2+y_F^2\right)\right)}{\sqrt{\det(\mathbf{Q_m^i})}}$$
$$\times\exp\left(\frac{jk_2}{2}\left\{\begin{bmatrix}\frac{x_F}{F}\\ \frac{y_F}{F}\end{bmatrix}^t\mathbf{Q_m^{i-1}}\begin{bmatrix}\frac{x_F}{F}\\ \frac{y_F}{F}\end{bmatrix}+2x_m\frac{x_F}{F}\right\}\right) \tag{25}$$

Total field is reformed as a geometrical series so that the FSR can be calculated. We eliminate the common terms in the geometrical series description of final field in the focal plane:

$$\sum_m\exp\left\{-j2(m-1)k_1\frac{d}{\cos(\theta_i)}-jk_2Z_{Pm}\right.$$
$$\left.+\frac{jk_2}{2}\left\{\mathbf{Q_m^{i-1}}(1,1)\left(\frac{x_F}{F}\right)^2+2x_m\left(\frac{x_F}{F}\right)\right\}\right\}\mathbf{Q_m^{i-1}}(1,1)$$
$$=\frac{\mathbf{Q_m^i}(2,2)}{\det(\mathbf{Q_m^i})}=\cos^2(\alpha_3)q_{x_{3m}}+\sin^2(\alpha_3)q_{y_{3m}} \tag{26}$$

The final field can be calculated in terms of output angle with the paraxial approximation $\tan(\frac{x_F}{F})\cong(\frac{x_F}{F})=\theta_F$. Finding the phase matching condition is not possible for general case of polarization due to nonlinear dependence. For special case of circular polarization, we have:

$$\alpha_3=\frac{\pi}{2}\Rightarrow\mathbf{Q_m^{i-1}}(1,1)=q_{y_{3m}}=\frac{n_2}{n_1}\{q_0+2(m-1)l\} \tag{27}$$

So the phase matching condition is:

$$\exp\left\{jk_0d\left\{\frac{2n_1}{\cos(\theta_i)}-2n_2\tan(\theta_i)\cos(\varphi)-2n_2\tan(\theta_i)\sin(\varphi)\theta_F-\frac{n_2^2}{n_1\cos(\theta_i)}\theta_F^2\right\}\right\}=1 \tag{28}$$

Assuming that the beams make zero angles with the horizontal direction, referring to the Figure 2, we have $\theta_t=\frac{\pi}{2}-\varphi$. So, FSR can be calculated from the following relation (for air-filled VIPA, where $n_2=1$):

$$\mathrm{FSR}=\frac{c}{2d\left\{n_1\cos(\theta_i)-\tan(\theta_i)\cos(\theta_t)\theta_F-\frac{\theta_F^2}{2n_1\cos(\theta_i)}\right\}} \tag{29}$$

2.3.2. 3-dB Bandwidth (Full-width at Half Maximum)

Other dominating figure of merit is FWHM or 3-dB bandwidth. That is the band- width that the output transmission spectrum reaches its half of its maximum. Based on etalon analysis [15], we have (Rr is the multiplication of two reflection coefficients of VIPA surfaces.):

$$\begin{cases} \text{FWHM} = \dfrac{c}{2\pi d\cos(\theta_i)}\dfrac{1-Rr}{\sqrt{Rr}} & \text{(Frequency)} \\ \text{FWHM} = \dfrac{\lambda_0^2}{2\pi d\cos(\theta_i)}\dfrac{1-Rr}{\sqrt{Rr}} & \text{(Wavelength)} \end{cases} \tag{30}$$

The finesse parameter is $\frac{\pi\sqrt{Rr}}{1-Rr}$ considering VIPA's similarities with etalon. The incident angle is determined from the following formula regarding the phase matching condition at the origin for the central wavelength:

$$m\lambda_0 = 2d\cos(\theta_i) \tag{31}$$

3. NUMERICAL RESULTS

3.1. Comparison of Current Work with Ref. [7]

According to the principles of phased arrays, the device acts as a beam former and prefers some angles to others as suggested by radiation pattern illustrated in Figure 4 for uniform and graded reflection profiles. It also demonstrates the VIPA's spatial filtering function that conforms to its application as a spectral disperser. There are other peaks in radiation pattern that shows other angles also satisfy phase matching condition. It is obvious that Shirasaki [7] limited the radiation pattern study to the main lobe, considered it as the reference direction and neglected the side lobes. (Refer to [17] for parameter values). Meanwhile, radiation peaks are invariant of profile engineering (Figure 4).

Figure 5(a) shows better characteristics and performance of graded reflection profile over the uniform one first proposed by Shirasaki [7]. The radiation patterns are compared in Figure 5 that illustrates higher contrast ratio of graded versus uniform profile. The graded one benefits from reduction of channel crosstalk in a demultiplexer setup and increased coupling efficiency to the fiber. The higher coupling efficiency will lead to lower insertion loss of VIPA in a demultiplexer scheme as well as better power efficiency. The coupling coefficient is derived through calculating overlap integral (Eq. (32)) where $U_F(v)$ is the output spatial pattern of VIPA demultiplexer and $G(v)$ is the input Gaussian spatial pattern of a single-mode fiber with

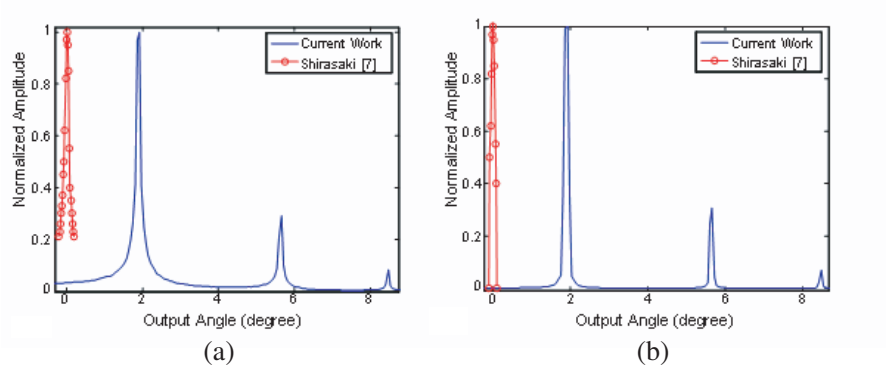

Figure 4. Comparison of VIPA profiles after the lens with [7] for (a) uniform and (b) graded profiles.

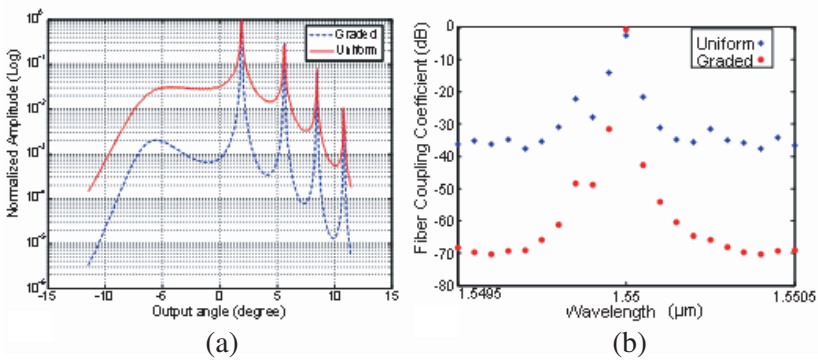

Figure 5. Comparison of (a) VIPA radiation patterns after the lens for uniform and graded profiles. (b) Coupling coefficient efficiency for uniform and graded profiles using [7] parameters.

diameter of 15 μm. The coupling coefficient vs. wavelength deviations is plotted in Figure 5(b) that clarifies the higher wavelength selectivity of graded over the uniform one. This behavior results in the mentioned reduced channel crosstalk.

$$\text{Coupling} = \frac{\left|\int U_F(v)G^*(v)dv\right|^2}{\int |U_F(v)|^2\,dv \int |G(v)|^2\,dv} \tag{32}$$

Comparison of output 3D radiation patterns on the lens focal plane confirms the aforementioned better performance of graded profile over the uniform one in the application of demultiplexer (Figures 6(a) and (b)). The graded one has more side lobes (which can be employed

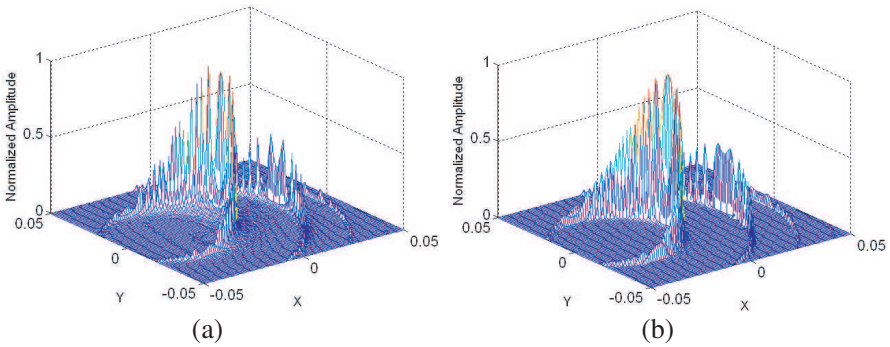

Figure 6. Comparison of 3-D radiation pattern of VIPA demultiplexer on the lens focal plane for (a) uniform and (b) graded profiles (X and Y are both in meter) using [7] parameters.

for more demultiplexer channel allocation) and it also benefits from higher contrast ratio. Despite the radial symmetry of spherical lens, the output patterns lack it due to the radial asymmetry of VIPA spectral disperser pattern.

Employing 3D pattern instead of 2D one increases the number of available codes in an optical Code Division Multiple Access (CDMA) scheme. Consequently, assigning 2D codes to users will dramatically improve the number of coverable users [24]. Because selection of codes in a 2D plane adds a degree of freedom, the demultiplexer channels can be discriminated so that the channel crosstalk is substantially reduced. This channel crosstalk decrement translates into the lower multi-user interference (MUI) which is a key factor in enhancement of CDMA networks [24].

3.2. Comparison of Current Work with Ref. [15]

Deviation of detector from the focal plane is studied in [15] referred as "spatial chirp effect". The result of the deviation of detector from the focal plane (± 2 mm) is shown in Figure 7 in linear and logarithmic scale. Detuning from the focal plane to the farther (nearer) distances from the lens will degrade the transmission spectrum of VIPA as well as shifting the peak to lower (higher) wavelengths. As Eq. (17) suggests even if we place the detector on the focal plane, there remains a non-quadratic phase for 3D analysis in contrast to the previous 2D analysis [15]. Our proposed formulation holds true for arbitrary deviations from the focal plane.

The ratio of FSR (here, 0.8 nm)/FHWM (here, 4.18 pm) is a

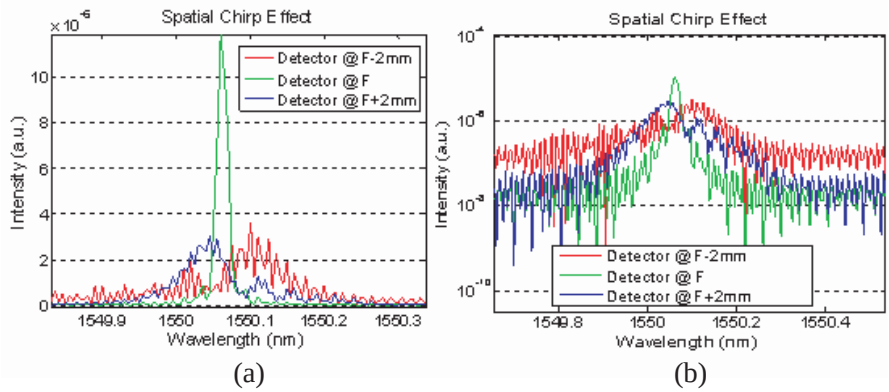

Figure 7. Transmission spectrum variations by detector place detuning (spatial chirp effect) (±2 mm) [15] (a) linear and (b) logarithmic scale.

measure of adjustable wavelength channels (about 190). Increasing this ratio will increase the number of WDM channels as well as channel crosstalk (indeed, it is required to carefully engineer the reflection profile or other design parameters to compensate for it); hence, improvement in communication system throughput.

4. CONCLUSION

We have proposed a rigorous vectorial Gaussian beam tracing method to extract a 3D generalized analytic model for the VIPA pattern after the lens in a closed-form formulation. To our knowledge, this is the first VIPA demultiplexer 3D performance analysis with arbitrary polarization input Gaussian beam at an arbitrary vertical plane using a generalized imaging lens system. The comparisons with previously-published 2D results show a good agreement. The advantages and potentials of the proposed method were also investigated previously in [17] repeated here for convenience: 1) The source beam waists are finite in both directions that are modeled as a generalized elliptic vectorial Gaussian beam. 2) The vectorial behavior of electromagnetic fields is modeled precisely by vectorial reflection and transmission coefficients. 3) This method can handle both types of VIPA (air-filled $n_2 = 1$ and solid $n_2 = n > 1$ and moreover, the device in the arbitrary environment by selecting n_1 and n_3). 4) The restricting assumptions like scalar formulation, negligence of wave's polarization and setup's misalignments are eliminated. 5) Demultiplexer pattern

is derived not only at focal plane but also at arbitrary distance after the lens. Having exact description of 3D output pattern of device, features such as reflection profile of VIPA and distance from the lens can be employed to design and optimize a setup for the aforementioned applications such as femtosecond pulse shaping, arbitrary waveform generation and OCDMA encoding/decoding. Furthermore, the results can fully predict the performance of VIPA demultiplexer general setup and effects of design parameter variations.

REFERENCES

1. Lipson, J., W. J. Minford, E. J. Murphy, T. C. Rice, R. A. Linke, and G. T. Harvey, "A six-channel wavelength multiplexer and demultiplexer for single mode systems," *IEEE J. Lightwave Technol.*, Vol. 3, 1159–1163, 1985.
2. Okamoto, K., "Recent progress of integrated optics planar lightwave circuits," *Opt. Quantum Electron.*, Vol. 31, 107–129, 1999.
3. Park, S. J., C. H. Lee, K. T. Jeong, H. J. Park, J. G. Ahn, and K. H. Song, "Fiber-to-the-Home services based on wavelength-division-multiplexing passive optical networks," *IEEE J. Lightwave Technol.*, Vol. 22, No. 11, 2582–2591, 2004.
4. Shirasaki, M., "Large angular dispersion by a virtually imaged phased array and its application to a wavelength demultiplexer," *Optics Letters*, Vol. 21, 366–368, 1996.
5. Shirasaki, M., "Chromatic-dispersion compensator using virtually imaged phased array," *IEEE Photon. Technol. Lett.*, Vol. 9, 1598–1560, 1997.
6. Shirasaki, M., "Compensation of chromatic dispersion and dispersion slope using a virtually imaged phased array," *OFC'01*, 2001.
7. Shirasaki, M., A. N. Akhter, and C. Lin, "Virtually imaged phased array with graded reflectivity," *IEEE Photon. Technol. Lett.*, Vol. 11, 1443–1445, 1999.
8. Leaird, D. E. and A. M. Weiner, "Femtosecond direct space-to-time pulse shaping," *IEEE J. of Quantum Electronics*, Vol. 37, No. 4, 494–504, 2001.
9. Etemad, S., T. Banwell, S. Galli, J. Jackel, R. Menendez, P. Toliver, J. Young, P. Delfyett, C. Price, and T. Turpin, "Optical-CDMA incorporating phase coding of coherent frequency bins: Concept, simulation, experiment," *OFC'04*, FG5, 2004.
10. Xiao, S., J. D. McKinney, and A. M. Weiner, "Photonic microwave

arbitrary waveform generation using a vipa direct space-to-time pulse shaper," *IEEE Photon. Technol. Lett.*, Vol. 16, No. 8, 1936–1938, 2004.

11. Lee, G. and A. M. Weiner, "Programmable optical pulse burst manipulation using a VIPA based fourier transform pulse shaper," *IEEE J. Lightwave Technol.*, Vol. 23, No. 11, 3916, 2005.
12. Yang, L., "Analytical treatment of virtual image phase array," *OFC'02*, 321–322, Anaheim, CA, 2002.
13. Vega, A., A. M. Weiner, and C. Lin, "Generalized grating equation for virtually-imaged phased-array spectral dispersers," *Appl. Opt.*, Vol. 42, No. 20, 4152–4155, 2003.
14. Xiao, S., A. M. Weiner, and C. Lin, "A dispersion law for virtually imaged phased-array spectral dispersers based on paraxial wave theory," *IEEE J. of Quantum Electronics*, Vol. 40, No. 4, 420–426, 2004.
15. Xiao, S., A. M. Weiner, and C. Lin, "Experimental and theoretical study of hyperfine WDM demultiplexer performance using the virtually imaged phased-array (VIPA)," *IEEE J. Lightwave Technol.*, Vol. 23, No. 3, 1456, 2005.
16. Mokhtari, A. and A. A. Shishegar, "A rigorous vectorial Gaussian beam modeling of virtually-imaged-phased-arrays," *AOE'07*, 514–516, 2007.
17. Mokhtari, A. and A. A. Shishegar, "Rigorous vectorial Gaussian beam modeling of spectral dispersing performance of virtually imaged phased arrays," *J. Opt. Soc. Am. B*, Vol. 26, No. 2, 272–278, 2009.
18. Goodman, J. W., *Introduction to Fourier Optics*, 77–96, McGraw-Hill, San Francisco, CA, 1968.
19. Haus, H. A., *Waves and Fields in Optoelectronics*, Prentice-Hall, Englewood Cliffs, NJ, 1984.
20. Ramo, S., *Fields and Waves in Communication Electronics*, John Wiley & Sons, 1994.
21. Verdeyen, J. T., *Laser Electronics*, Prentice Hall, 1995.
22. Arnaud, J. A. and H. Kogelnik, "Gaussian light beams with general astigmatism," *Applied Optics*, Vol. 8, No. 8, 1687–1694, 1969.
23. Iizuka, K., *Elements of Photonics, Fabry-perot Resonator Beams and Radiation Pressure*, Vol. 1, Chap. 3, 181, Wiley Interscience, 2002.
24. Prucnal, P. R., *Optical Code Division Multiple Access: Fundamentals and Applications*, CRC Press, New York, 2006.